A&A 665, L8 (2022)
https://doi.org/10.1051/0004-6361/202142562

Astronomy & Astrophysics

LETTER TO THE EDITOR

Kiloparsec view of a typical star-forming galaxy when the Universe was ∼1 Gyr old

II. Regular rotating disk and evidence for baryon dominance on galactic scales

R. Herrera-Camus[1], N. M. Förster Schreiber[2], S. H. Price[2], H. Übler[3,4], A. D. Bolatto[5], R. L. Davies[6,7], D. Fisher[6,7], R. Genzel[2], D. Lutz[2], T. Naab[8], A. Nestor[9], T. Shimizu[2], A. Sternberg[2,9,10], L. Tacconi[2], and K. Tadaki[11]

[1] Departamento de Astronomía, Universidad de Concepción, Barrio Universitario, Concepción, Chile
e-mail: rhc@astro-udec.cl
[2] Max-Planck-Institut für Extraterrestische Physik (MPE), Giessenbachstr., 85748 Garching, Germany
[3] Cavendish Laboratory, University of Cambridge, 19 J.J. Thomson Avenue, Cambridge CB3 0HE, UK
[4] Kavli Institute for Cosmology, University of Cambridge, Madingley Road, Cambridge CB3 0HA, UK
[5] Department of Astronomy, University of Maryland, College Park, MD 20742, USA
[6] Centre for Astrophysics and Supercomputing, Swinburne Univ. of Technology, PO Box 218, Hawthorn, VIC 3122, Australia
[7] ARC Centre of Excellence for All Sky Astrophysics in 3 Dimensions (ASTRO 3D), Australia
[8] Max-Planck Institute for Astrophysics, Karl Schwarzschildstrasse 1, 85748 Garching, Germany
[9] School of Physics and Astronomy, Tel Aviv University, Ramat Aviv 69978, Israel
[10] Center for Computational Astrophysics, 162 5th Ave., New York, NY 10010, USA
[11] National Astronomical Observatory of Japan, 2-21-1 Osawa, Mitaka, Tokyo 181-8588, Japan

Received 2 November 2021 / Accepted 16 February 2022

ABSTRACT

We present a kinematic analysis of the main-sequence galaxy HZ4 at $z = 5.5$. Our study is based on deep, spatially resolved observations of the [C II] 158 µm transition obtained with the Atacama Large Millimeter/Submillimeter Array (ALMA). From the combined analysis of the disk morphology, the 2D velocity structure, and forward modeling of the 1D velocity and velocity dispersion profiles, we conclude that HZ4 has a regular rotating disk in place. The intrinsic velocity dispersion in HZ4 is high ($\sigma_0 = 65.8^{+2.9}_{-3.3}$ km s^{-1}), and the ratio between the rotational velocity and the intrinsic velocity dispersion is $V_{\rm rot}/\sigma_0 = 2.2$. These values are consistent with the expectations from the trends of increasing σ_0 and decreasing $V_{\rm rot}/\sigma_0$ as a function of the redshift observed in main-sequence galaxies up to $z \approx 4$. Galaxy evolution models suggest that the high level of turbulence observed in HZ4 can only be achieved if, in addition to stellar feedback, there is radial transport of gas within the disk. Finally, we find that HZ4 is baryon-dominated on galactic scales ($\lesssim 2 \times R_{\rm e}$), with a dark-matter fraction at one effective radius of $f_{\rm DM}(R_{\rm e}) = 0.41^{+0.25}_{-0.22}$. This value is comparable to the dark-matter fractions found in lower redshift galaxies that could be the descendants of HZ4: massive ($M_\star \approx 10^{11}\,M_\odot$), star-forming galaxies at $z \sim 2$, and passive, early-type galaxies at $z \approx 0$.

Key words. galaxies: high-redshift – galaxies: kinematics and dynamics – galaxies: structure – galaxies: ISM

1. Introduction

The study of galaxy kinematics can provide answers to some of the most fundamental questions about galaxy formation and evolution. These include determining the epoch when galaxies form their disks, the distribution of baryon and dark matter within galaxies, and the dynamical state of galaxies as a function of cosmic time. From early kinematic analyses of nearby galaxies (e.g., Rubin & Ford 1970; Sofue & Rubin 2001), to more recent studies of high redshift systems thanks to powerful interferometers and integral-field unit (IFU) systems, especially with adaptive optics (e.g., Förster Schreiber & Wuyts 2020), we can now start connecting the kinematic properties of the very early galaxies to their likely descendants.

Based on deep, spatially resolved observations of the Hα and CO transitions in star-forming galaxies between $0 \lesssim z \lesssim 3$, we have learned that: (1) the amount of turbulence in the interstellar medium (ISM) – measured by the intrinsic gas velocity dispersion – increases as a function of redshift (e.g., Genzel et al. 2006; Förster Schreiber et al. 2006; Cresci et al. 2009; Kassin et al. 2012; Stott et al. 2016; Johnson et al. 2018; Übler et al. 2019); (2) galaxy disks are more dynamically turbulent (or dynamically hot) at higher redshift, quantified by the ratio between the rotational velocity and the intrinsic velocity dispersion (e.g., Law et al. 2009; Förster Schreiber et al. 2009; Simons et al. 2017; Wisnioski et al. 2015, 2019); and (3) more than half of the massive, star-forming galaxies at $z \sim 1{-}2$ are baryon-dominated on galactic scales (e.g., Wuyts et al. 2016; Lang et al. 2017; Übler et al. 2018; Genzel et al. 2017, 2020; Price et al. 2021). These observational results point to the importance of stellar feedback, clump formation, and gas transport in the evolution of galaxies (e.g., Dekel & Burkert 2014; Ostriker & Shetty 2011; Bournaud et al. 2014; Krumholz et al. 2018).

Article published by EDP Sciences

The kinematic properties of star-forming galaxies at $z \gtrsim 4$ remain relatively unexplored. This situation, however, is rapidly changing, thanks to observations of the [C II] 158 µm fine-structure line. The [C II] transition originates from the collisional excitation of C^+ ions by electrons, H_2 molecules, and – to the advantage of kinematic studies – H atoms. For now, observations of the H I 21 cm line in high redshift galaxies are out of reach. This makes the [C II] transition an excellent alternative to trace the outer disk of distant galaxies (e.g., de Blok et al. 2016; Fujimoto et al. 2019, 2020; Herrera-Camus et al. 2021).

Between $z \sim 4$–6, a morpho-kinematic analysis of 29 star-forming galaxies based on [C II] line observations, with modest angular resolution (∼1″ or ∼6.5 kpc at $z = 5$), indicates a diversity of kinematic types, including rotators, dispersion-dominated systems, and mergers (Jones et al. 2021). This result is confirmed by the handful of spatially resolved [C II] observations available for typical star-forming galaxies probing the main-sequence population in the stellar mass ($M_\star$) – star formation rate (SFR) plane at $z \gtrsim 4$. Evidence for rotating disks has been found in two Lyman break galaxies at $z \approx 6.8$ (Smit et al. 2018), one absorption-selected galaxy at $z = 4.2$ (Neeleman et al. 2020), and a five dusty, star-forming galaxies at $z \approx 4$ (Rizzo et al. 2020, 2021). There are also examples of complex kinematics, including a potential interaction between three systems (Riechers et al. 2013) and two star-forming galaxies in the process of merging (Ginolfi et al. 2020). In the near future, the Atacama Large Millimeter/Submillimeter Array (ALMA), the Northern Extended Millimeter Array (NOEMA), and the *James Webb* Space Telescope (JWST) will continue to contribute to the rapid increase in kinematic studies of high-redshift, star-forming galaxies.

In this Letter, we present one of the most complete kinematic analyses to date of a main-sequence, star-forming galaxy at $z \approx 5$. For this, we use deep, spatially resolved [C II] line observations of the star-forming galaxy HZ4 at $z = 5.5$ ($M_\star = 10^{10.15}\,M_\odot$, SFR $= 40.7\,M_\odot\,\mathrm{yr}^{-1}$; Faisst et al. 2020). The observations and the analysis of the morphology, ISM, extended emission (or "halo"), and outflow properties of HZ4 are presented in Herrera-Camus et al. (2021, hereafter Paper I).

2. Observations and data reduction

For a detailed description of the observations and data reduction, we refer to Paper I. HZ4 was observed with ALMA for a total of 8.4 h (4.7 h on source) as part of project 2018.1.01605.S (PI: Herrera-Camus). The observations were carried out in the C34-4 configuration in Band 7. The data were processed using the Common Astronomy Software Applications package (CASA; McMullin et al. 2007) version 5.6.2. Using the CASA task `tclean` and the Multi-Scale CLEAN algorithm (Cornwell 2008), we generated a [C II] cube with a synthesized beam size of $\theta_{\mathrm{beam}} = 0.39'' \times 0.34''$. The velocity resolution of the [C II] cube is 16 km s^{-1}. This is at least a factor ∼4 higher than the best spectral resolution that can be achieved in near-infrared observations, so the line spread effect is negligible.

3. Results and analysis

3.1. Basic kinematic properties

We created 2D kinematic maps of HZ4 by fitting a Gaussian profile to the [C II] line emission in each pixel and by accounting for the systemic velocity. Figure 1 shows the resulting velocity field (first moment; top left) and the velocity dispersion map (second moment; top right). The kinematic center is defined from the combination of the centrally peaked velocity dispersion and the location of the steepest gradient in the velocity field, resulting in the position RA +09:58:28.5 and Dec +02:03:06.3 (gray cross in Fig. 1). The major kinematic axis is determined from the 2D velocity field as the angle at which the radial velocity profile, centered in the kinematic center, includes the largest observed velocity difference. This results in a position angle (PA) of 200° measured anticlockwise from north to the receding side of the galaxy (or 20° measured east of north; gray line in Fig. 1).

Based on a an initial kinematic analysis, we find that HZ4 fulfills, at minimum, four main characteristics of a rotating disk as described in Förster Schreiber & Wuyts (2020). First, there is a smooth velocity gradient observed across the galaxy. Second, the kinematic major axis is aligned with the [C II] morphological major axis, which has a PA = 17.7° measured east from north (Paper I). Third, HZ4 has a centrally peaked velocity dispersion distribution. Fourth, the kinematic center and the morphological center (see Paper I) are spatially coincident, separated by a projected distance of only ∼0.2″ (∼1 kpc), which is smaller than the beam size. These basic kinematic properties suggest that HZ4 has a smooth, rotating disk in place at $z \approx 5.5$. The modeling and discussion of the kinematics properties of HZ4 are presented in Sect. 4.

3.2. Rotation curve and velocity dispersion profile

We constructed the rotation curve and velocity dispersion profile from the [C II] cube by placing 0.4″ diameter apertures (approximate beam size) along the kinematic major axis, separated every ∼0.1″. We emphasize that for the purpose of our analysis, the major-axis information provides the strongest constraints on the disk models we used (see Sect. 3.3). The resulting velocity and dispersion profiles are shown in the bottom panels of Fig. 1.

The rotation curve of HZ4 is more extended in the northeast (approaching) side, and reaches out to ∼1″. This corresponds to a projected physical distance of ∼6 kpc, or ∼2× the effective radius R_e (as measured from fitting an exponential disk profile to the integrated [C II] emission, Paper I). The rotation curve peaks at an observed projected velocity of 80 km s^{-1} at a distance of $\sim 1.2 \times R_e$ from the center, and then drops down to 60 km s^{-1} at $\sim 2 \times R_e$. Dropping rotation curves have also been observed in massive, star-forming galaxies at $z \sim 1$–2 (Genzel et al. 2017, 2020; Lang et al. 2017). As we discuss in more detail in Sect. 4, these can be interpreted as the combination of low central dark-matter fractions and/or the effect of asymmetric drift due to high intrinsic velocity dispersions (e.g., Burkert et al. 2010).

3.3. Kinematic modeling

We simultaneously modeled the velocity and velocity dispersion profiles extracted along the major kinematic axis using an updated version of the fully 3D parametric code DYSMAL (Cresci et al. 2009; Davies et al. 2011; Wuyts et al. 2016; Übler et al. 2018; Price et al. 2021). DYSMAL uses a forward-modeling approach and accounts for all important observational effects, including spatial beam smearing. The code creates a 3D mass model, forward model to produce a 3D spectroscopy cube, from which we extracted the 1D profiles in the same fashion as the observations. These were then compared to the data using a Markov chain Monte Carlo (MCMC) sampling procedure (`EMCEE`, Foreman-Mackey et al. 2013). A detailed description of the DYSMAL modeling of the HZ4 data can be found in Appendix A. Free parameters in our modeling are the total

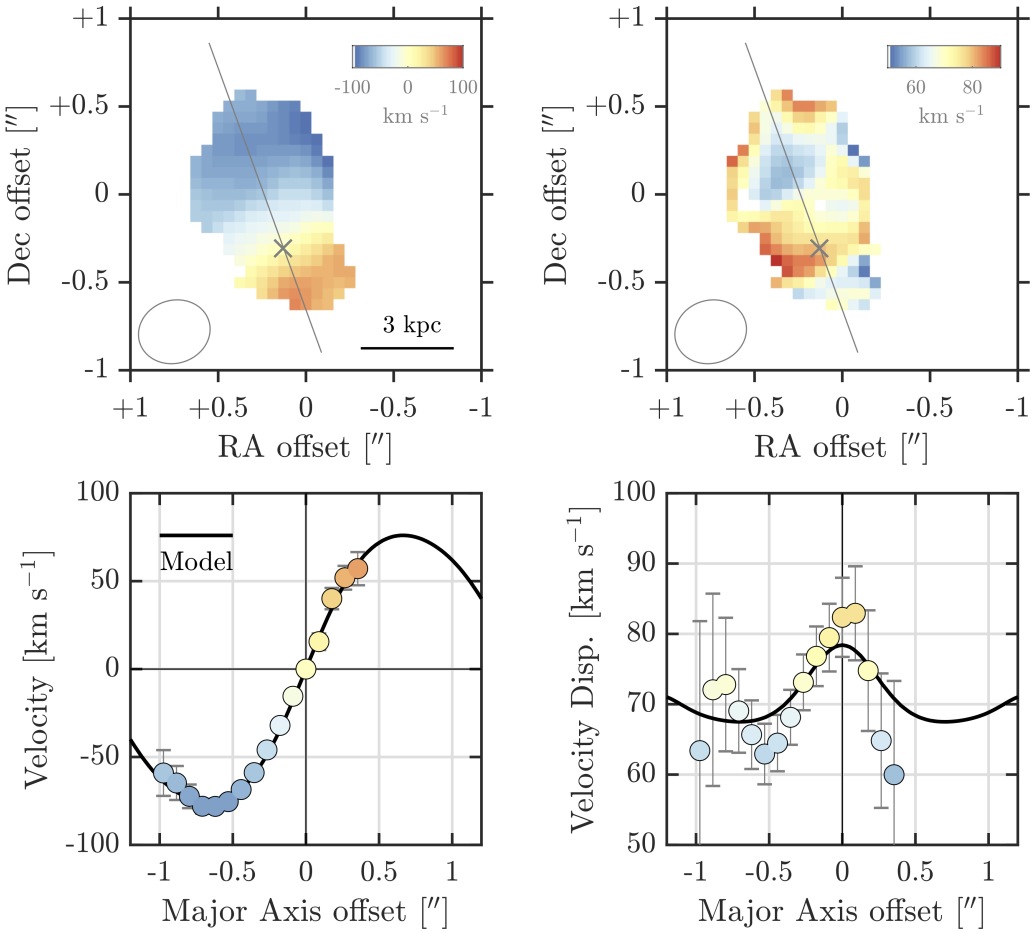

Fig. 1. Kinematic structure of HZ4 as traced by the [C II] line emission. *Top*: [C II] velocity field (*left*) and velocity dispersion map (*right*) of HZ4. The ALMA synthesized beam ($\theta = 0.39'' \times 0.34''$) is shown in the bottom-left corner. *Bottom*: rotation curve and velocity dispersion profiles extracted employing a pseudo-slit oriented along the kinematic major axis shown by the gray solid line in the *upper panels*, where the kinematic center is shown with a gray cross. The solid black line in both panels represents the best-fit DYSMAL model beam-convolved to the observed space.

baryonic mass ($M_{\rm bar}$), the effective radius ($R_{\rm e}$), the intrinsic velocity dispersion (σ_0), and the enclosed dark-matter fraction within one effective radius ($f_{\rm DM}(R_{\rm e})$). From the MCMC analysis, the maximum a posteriori values of the free parameters (found by jointly analyzing the posteriors of all free parameters) are the following: $\log_{10}(M_{\rm bar}/M_\odot) = 10.38^{+0.25}_{-0.13}$, $R_{\rm e} = 3.4^{+0.5}_{-0.3}$ kpc, $f_{\rm DM}(R_{\rm e}) = 0.41^{+0.25}_{-0.22}$, and $\sigma_0 = 65.8^{+2.9}_{-3.3}$ km s^{-1}. We consider these parameters as the model that best describe our data. The corresponding model velocity and velocity dispersion profiles in the observed space are shown as black solid lines in Fig. 1. The resulting baryonic mass translates into a high model-based gas fraction of $M_{\rm gas}/M_\star = (M_{\rm bar} - M_\star)/M_\star = 0.7$, comparable to the mean [C II]-based gas mass fraction measured in main-sequence, star-forming galaxies between $5.1 < z < 5.9$ (Dessauges-Zavadsky et al. 2020).

4. Discussion

4.1. Velocity dispersion and disk stability over cosmic time

The intrinsic gas velocity dispersion of main-sequence star-forming galaxies has been observed to increase as a function of redshift at least up to $z \sim 4$ (e.g., Förster Schreiber et al. 2006; Kassin et al. 2007; Genzel et al. 2011; Wisnioski et al. 2015; Turner et al. 2017; Simons et al. 2017; Johnson et al. 2018; Übler et al. 2019; Livermore et al. 2015). This evolution is consistent with the observed increase in the molecular gas fractions with redshift (e.g., Tacconi et al. 2020): if galaxy disks grow in a marginally stable equilibrium state with Toomre parameter $Q \sim 1$, then it is expected that $V_{\rm rot}/\sigma_0 \propto 1/f_{\rm gas}$ (e.g., Genzel et al. 2011; Glazebrook 2013; Wisnioski et al. 2015).

Figure 2 shows the evolution of σ_0 observed in main-sequence galaxies as a function of redshift. The points correspond to the averages of several galaxy surveys and individual measurements in the ionized and atomic and/or molecular gas, measured and/or compiled by Übler et al. (2019). The high intrinsic velocity dispersion inferred from the kinematic modeling of HZ4 ($\sigma_0 \approx 65$ km s^{-1}) is consistent with the extrapolation up to redshift $z \approx 5$ of the scaling relations derived for main-sequence galaxies. This is in line with the expectations from the observed increase in the cold gas fraction with redshift (Tacconi et al. 2018, 2020), of which HZ4 is no exception with a cold gas mass fraction of $M_{\rm gas}/M_\star = 0.7$ at $z \approx 5.5$.

We note that $V_{\rm rot}/\sigma_0$ is a measure of the dynamical support contributed by rotation versus random motions. We inferred from the kinematic modeling a value of $V_{\rm rot}/\sigma_0 = 2.2$. As Fig. 2 shows, this value is consistent with the evolution observed in main-sequence galaxies (Wisnioski et al. 2015, 2019, and references therein), and it is above the threshold assumed for an equal contribution to the dynamical support of disks

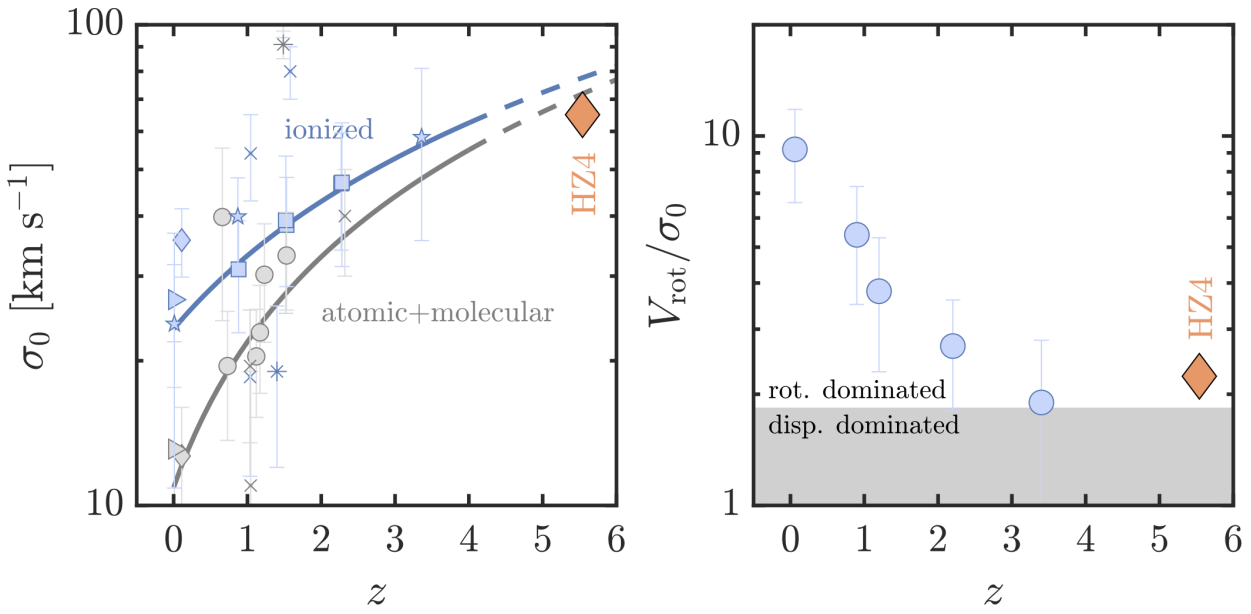

Fig. 2. Evolution of the intrinsic velocity dispersion (σ_0; *left*) and the disk dynamical support ($V_{\rm rot}/\sigma_0$; *right*) as a function of redshift. HZ4 at $z \approx 5$ is shown as an orange diamond. *Left panel*: circles show average values from different surveys of ionized (blue) and atomic and/or molecular gas (gray). These include the following: DYNAMO (diamonds; Fisher et al. 2019; Girard et al. 2021); HERACLES, THINGS, and EDGE (triangles; Leroy et al. 2008, 2009; Mogotsi et al. 2016; Bolatto et al. 2017); KMOS^{3D} and SINS/zC-SINF (squares; Förster Schreiber et al. 2006, 2009; Wisnioski et al. 2015, 2019; Übler et al. 2019); PHIBSS (circles; Tacconi et al. 2013; Freundlich et al. 2019); and GHASP/KDS/KROSS (stars; Epinat et al. 2010; Stott et al. 2016; Turner et al. 2017; Johnson et al. 2018). We also added individual measurements from lensed systems (crosses) from Swinbank et al. (2011) and Girard et al. (2019), as well as unlensed systems (asterisks) from Molina et al. (2019) and Übler et al. (2018). The solid lines show the best-fit relations to the observations compiled by Übler et al. (2019) up to $z \approx 3.5$. *Right panel*: the circles show the average values for $V_{\rm rot}/\sigma_0$ from the ionized gas measured and compiled by Wisnioski et al. (2015). The gray box shows the region below $V_{\rm rot}/\sigma_0 = \sqrt{3.36}$, where the contribution to the dynamical support of the disk by random motions starts to dominate (e.g., Förster Schreiber & Wuyts 2020).

from rotation and random motions ($V_{\rm rot}/\sigma_0 \approx \sqrt{3.36}$; e.g., Förster Schreiber & Wuyts 2020). The $V_{\rm rot}/\sigma_0$ value measured in HZ4, combined with the kinematic properties discussed in Sect. 3.1, provide one of the strongest pieces of evidence to date of the existence of regular rotating disks when the Universe was only ∼1 Gyr old.

To date, there have been few studies that have found evidence for rotating disks in the early Universe (e.g., Smit et al. 2018; Neeleman et al. 2020; Lelli et al. 2021; Rizzo et al. 2020, 2021). Interestingly, studies from Lelli et al. (2021), Rizzo et al. (2021), and Fraternali et al. (2021) conclude that the dusty starbursts in their samples are dynamically cold, with $V_{\rm rot}/\sigma_0$ values in the ∼7−30 range. As opposed to the case of HZ4, these values significantly exceed the expectations from the observed evolution of $V_{\rm rot}/\sigma_0$ for main-sequence galaxies in the range $z \approx 0$−4 (see Fig. 2). These differences could indeed reflect in part the different nature of the sources, with most of the Rizzo et al. (2021), Lelli et al. (2021), and Fraternali et al. (2021) targets (6 of the 8) lying at least an order of magnitude above the main sequence and typically being very compact compared to HZ4 and other galaxies close to the main sequence. We caution, however, that direct comparisons are also complicated by the different modeling approaches between the studies, and notably in the σ_0 parameterization, which is radially constant in this work, but exponentially decreasing in Rizzo et al. (2020, 2021).

4.2. Dark-matter fraction on galactic scales

Recent observational evidence shows that a large fraction of massive, star-forming galaxies at $z \sim 1$−2 are strongly baryon-dominated on galactic scales (e.g., Wuyts et al. 2016; Übler et al. 2018; Genzel et al. 2017, 2020; Price et al. 2021). Measuring dark-matter fractions requires well-sampled rotation curves that extend beyond the effective and turnover radius. Up to $z \sim 2$, these outer rotation curves have been mainly obtained by observations of the Hα and CO transitions. In the case of HZ4, our deep [C II] line observations allowed us to trace the rotation curve beyond the turnover point (∼1.2×$R_{\rm e}$), and as far as ∼2×$R_{\rm e}$. This enabled a robust decomposition of the baryonic and dark-matter components of the rotation curve based on DYSMAL.

Figure 3 (left) shows the intrinsic (inclination-corrected) baryonic, dark matter, and total circular velocity profile of HZ4. The effective radius is shown with a green vertical line. We find that HZ4 is baryon-dominated within $R_{\rm e}$, and the baryon dominance prevails out to $\sim 2 \times R_{\rm e}$. The right panel of Fig. 3 shows the $f_{\rm DM}(R_{\rm e})$ of HZ4 in context with other galaxy populations. The blue line shows the best fit to the $z \approx 0$ late-type galaxies[1]. While low-mass galaxies tend to be dark-matter-dominated, more massive disks have lower dark-matter fractions. The red line shows the best fit to passive, early-type galaxies at $z \approx 0$, which are strongly baryon-dominated within one $R_{\rm e}$ (Cappellari 2016). The gray box shows the mean (± the standard deviation around the mean) of the dark-matter fraction measured in 41 massive ($M_\star \approx 10^{10.5}$−$10^{11}\,M_\odot$), main-sequence galaxies at $z \approx 1$−2 (Genzel et al. 2020).

At the same $v_{\rm circ}$, and noting the time difference in evolution of ∼12.5 Gyr, HZ4 has a dark-matter fraction in between the values from late-type (dark-matter-dominated) and early-type (baryon-dominated) galaxies at $z \approx 0$, and it is comparable to the mean value found in more massive ($M_\star \sim 10^{11}\,M_\odot$),

[1] The fit to $z \approx 0$ late-type galaxies from Genzel et al. (2020; and references therein) corresponds to the following: $f_{\rm DM,late-type} = 1-0.279 \times (v_{\rm circ} - 50.3\,{\rm km\,s^{-1}})/100\,{\rm km\,s^{-1}}$.

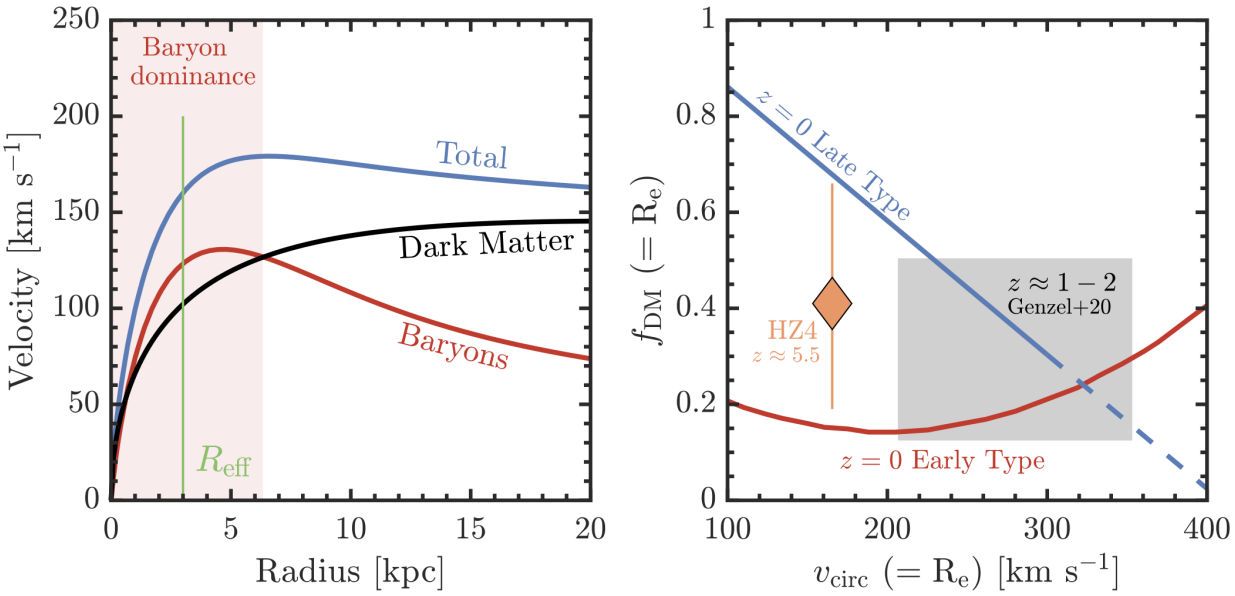

Fig. 3. Kinematic modeling of the rotation curve of HZ4. *Left*: intrinsic rotation curve (corrected by inclination) of HZ4 for baryons (red), dark matter (black), and total (blue) from the best-fit model. The green vertical line shows the $R_{\rm e}$, and the red colored box represents the spatial scales of baryon dominance in HZ4. *Right*: dark-matter fraction within $R_{\rm e}$ of HZ4 (orange diamond), main-sequence, star-forming galaxies at $z \approx 1$–2 (gray box; Genzel et al. 2020), and the best linear fit to $z \sim 0$ late-type galaxies (blue line), and $z \sim 0$ ATLAS-3D early-type galaxies (red curve; Cappellari 2016).

star-forming galaxies at $z \approx 2$. This is interesting because, from an abundance-matching perspective (e.g., Hill et al. 2017), the progenitors of the baryon-dominated, massive galaxies at $z \approx 2$ are $M_\star \approx 10^{10}\,M_\odot$ galaxies at $z \approx 5$, the stellar mass of HZ4. Therefore, one possibility is that the baryon dominance observed in massive, star-forming galaxies at cosmic noon is already in place at $z \approx 5$. This result is also supported by the Illustris-TNG simulations, which find only a mild evolution with redshift of the dark-mater fraction on galactic scales for a fixed stellar mass (Lovell et al. 2018). In fact, TNG galaxies at $z \approx 4$ with a similar stellar mass to HZ4 have a mean dark-matter fraction within one stellar half mass radius of $f_{\rm DM} \approx 0.4$, and this value only increases by 10–20% as galaxies grow to a stellar mass of $M_\star \approx 10^{11}\,M_\odot$ at $z \approx 2$.

4.3. Comparison to galaxy evolution models including feedback and gravity

Here we investigate what processes are responsible for the high intrinsic velocity dispersion observed in HZ4 using the state-of-the-art analytical model of galaxy evolution by Krumholz et al. (2018). We consider four model scenarios: (1) gas transport plus stellar feedback, (2) gas transport without stellar feedback, and two additional models of stellar feedback without gas transport, assuming (3) a fixed star formation efficiency per free-fall time ($\epsilon_{\rm ff} = 0.015$), and (4) a fixed Toomre parameter Q. Finally, for comparison with HZ4, we chose a set of parameters in the Krumholz et al. (2018) model that are representative of high-z galaxies[2].

Figure 4 shows the comparison between the measured σ_0 and SFR in HZ4, and the predictions from the four Krumholz et al. (2018) models. The blue lines correspond to the models that only consider stellar feedback. In the case where $\epsilon_{\rm ff}$ is fixed (dotted line), the model predicts a constant σ_0 of $\approx$20 km s^{-1}. If Q is fixed (dashed line), there is no σ_0 floor, but σ_0 only mildly increases with star formation activity. In both cases, stellar feedback alone is not capable of reproducing the high turbulence observed in HZ4. The situation is completely different with models that include radial transport of gas. The red and green lines show such models with and without including stellar feedback, respectively. For SFR $\lesssim 15\,M_\odot$ yr^{-1}, the main difference between the two models is the σ_0 floor of about $\approx$20 km s^{-1} in the

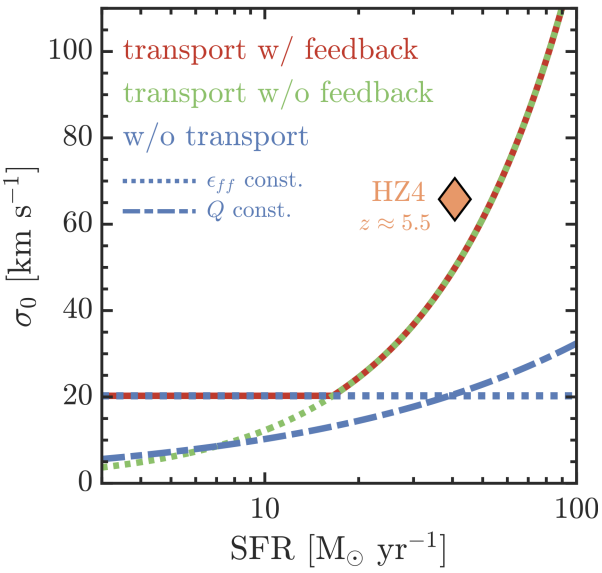

Fig. 4. Intrinsic velocity dispersion σ_0 as a function of the star formation rate (SFR) for HZ4 (orange diamond), and the unified models by Krumholz et al. (2018) for high-z galaxies that consider transport and feedback (red), only transport (green), and feedback without transport (blue): the dotted and dashed lines correspond to the models with constant $\epsilon_{\rm ff}$ and constant Q, respectively.

[2] These include a total circular velocity of 200 km s^{-1} measured at a distance of 5 kpc, and a molecular gas fraction of $M_{\rm gas}/M_\star = 0.75$, which is in good agreement with HZ4.

case where stellar feedback is included. For SFR $\gtrsim 15\,M_\odot\,\mathrm{yr}^{-1}$, both models are identical, and σ_0 increases rapidly with the SFR. At the SFR of HZ4, the radial transport models reproduce the high σ_0 measured in the system remarkably well.

One of the consequences of gas richness and efficient radial transport of gas and clumps inward is the formation of massive bulges, and the increase in nuclear gas outflows powered by central starbursts and active galactic nuclei (e.g., Elmegreen et al. 2008; Dekel & Krumholz 2013; Bournaud et al. 2014; Ceverino et al. 2015). In that sense, the presence of migrating gas in HZ4 suggested by the Krumholz et al. (2018) models is consistent with the low dark-matter fraction measured in the inner disk, and with the evidence of a centrally driven outflow (Paper I).

5. Conclusions

We have obtained deep, kiloparsec-scale resolution ALMA observations in the [C II] 158 µm transition of HZ4, a main-sequence galaxy at $z = 5.5$. The results are presented in two papers. In the first one (Paper I), we analyzed the ISM, outflow, and extended emission properties of the system. Here, we focus on the kinematics. The main results can be summarized as follows:

- Evidence for a regular rotating disk at $z = 5.5$: We simultaneously modeled the rotation curve and the velocity dispersion profile using the kinematic code DYSMAL. We measured an intrinsic velocity dispersion of $\sigma_0 = 65.8^{+2.9}_{-3.3}$ km s^{-1} and $V_{\rm rot}/\sigma_0 = 2.2$. The latter, combined with the smooth, monotonic velocity gradient observed across the galaxy, the alignment between the morphological and kinematic major axis, and a centrally peaked velocity dispersion profile, strongly suggest that HZ4 already has a regular rotating disk in place at $z = 5.5$, when the Universe was only ∼1 Gyr old.
- High intrinsic velocity dispersion and the importance of radial transport: The high intrinsic velocity dispersion measured in HZ4 is in agreement with the trends of increasing σ_0 with redshift observed in main-sequence galaxies up to $z \sim 4$. State-of-the art analytic galaxy evolution models by Krumholz et al. (2018) are only capable of reproducing the high intrinsic velocity dispersion observed in HZ4 if the radial transport of gas in addition to stellar feedback are included.
- Low dark-matter fraction on galactic scales: From the kinematic modeling, we find that HZ4 is baryon-dominated out to $\sim 2 \times R_{\rm e}$, with a dark-matter fraction at the effective radius $R_{\rm e}$ of $f_{\rm DM}(R_{\rm e}) = 0.41^{+0.25}_{-0.22}$. This low dark-matter fraction is comparable to that found in systems that could be the descendants of HZ4: massive ($M_\star \approx 10^{11}\,M_\odot$), star forming galaxies at $z \approx 2$ (e.g., Genzel et al. 2020), and passive, early-type galaxies at $z \approx 0$ (e.g., Cappellari 2016).

Future spatially resolved kinematics surveys of the main-sequence galaxy population at $z \sim 4$–5 are needed to draw statistically significant conclusions. This will be possible thanks to observations of the ionized gas with JWST, and upcoming surveys of the cold gas using the [C II] transition such as the ALMA Cycle 8 Large Program CRISTAL[3].

Acknowledgements. We thank the referee for very useful comments and suggestions that improved the manuscript. R.H.-C. thanks the Max Planck Society for support under the Partner Group project "The Baryon Cycle in Galaxies" between the Max Planck for Extraterrestrial Physics and the Universidad de Concepción. R.H.-C. also acknowledges financial support from Millenium Nucleus NCN19058 (TITANs) and support by the ANID BASAL projects ACE210002 and FB210003. H.Ü. gratefully acknowledges support by the Isaac Newton Trust and by the Kavli Foundation through a Newton-Kavli Junior Fellowship.

[3] https://www.alma-cristal.info

References

Bolatto, A. D., Wong, T., Utomo, D., et al. 2017, ApJ, 846, 159
Bournaud, F., Perret, V., Renaud, F., et al. 2014, ApJ, 780, 57
Burkert, A., Genzel, R., Bouché, N., et al. 2010, ApJ, 725, 2324
Cappellari, M. 2016, ARA&A, 54, 597
Ceverino, D., Dekel, A., Tweed, D., & Primack, J. 2015, MNRAS, 447, 3291
Cornwell, T. J. 2008, IEEE J. Sel. Top. Signal Process., 2, 793
Cresci, G., Hicks, E. K. S., Genzel, R., et al. 2009, ApJ, 697, 115
Davies, R., Förster Schreiber, N. M., Cresci, G., et al. 2011, ApJ, 741, 69
de Blok, W. J. G., Walter, F., Smith, J. D. T., et al. 2016, AJ, 152, 51
Dekel, A., & Burkert, A. 2014, MNRAS, 438, 1870
Dekel, A., & Krumholz, M. R. 2013, MNRAS, 432, 455
Dessauges-Zavadsky, M., Ginolfi, M., Pozzi, F., et al. 2020, A&A, 643, A5
Dutton, A. A., & Macciò, A. V. 2014, MNRAS, 441, 3359
Elmegreen, B. G., Bournaud, F., & Elmegreen, D. M. 2008, ApJ, 688, 67
Epinat, B., Amram, P., Balkowski, C., & Marcelin, M. 2010, MNRAS, 401, 2113
Faisst, A. L., Schaerer, D., Lemaux, B. C., et al. 2020, ApJS, 247, 61
Fisher, D. B., Bolatto, A. D., White, H., et al. 2019, ApJ, 870, 46
Foreman-Mackey, D., Hogg, D. W., Lang, D., & Goodman, J. 2013, PASP, 125, 306
Förster Schreiber, N. M., & Wuyts, S. 2020, ARA&A, 58, 661
Förster Schreiber, N. M., Genzel, R., Lehnert, M. D., et al. 2006, ApJ, 645, 1062
Förster Schreiber, N. M., Genzel, R., Bouché, N., et al. 2009, ApJ, 706, 1364
Fraternali, F., Karim, A., Magnelli, B., et al. 2021, A&A, 647, A194
Freundlich, J., Combes, F., Tacconi, L. J., et al. 2019, A&A, 622, A105
Fujimoto, S., Ouchi, M., Ferrara, A., et al. 2019, ApJ, 887, 107
Fujimoto, S., Silverman, J. D., Bethermin, M., et al. 2020, ApJ, 900, 1
Genzel, R., Tacconi, L. J., Eisenhauer, F., et al. 2006, Nature, 442, 786
Genzel, R., Newman, S., Jones, T., et al. 2011, ApJ, 733, 101
Genzel, R., Förster Schreiber, N. M., Übler, H., et al. 2017, Nature, 543, 397
Genzel, R., Price, S. H., Übler, H., et al. 2020, ApJ, 902, 98
Ginolfi, M., Jones, G. C., Béthermin, M., et al. 2020, A&A, 643, A7
Girard, M., Dessauges-Zavadsky, M., Combes, F., et al. 2019, A&A, 631, A91
Girard, M., Fisher, D. B., Bolatto, A. D., et al. 2021, ApJ, 909, 12
Glazebrook, K. 2013, PASA, 30, e056
Herrera-Camus, R., Förster Schreiber, N., Genzel, R., & Tacconi, L. 2021, A&A, 649, A31 (Paper I)
Hill, A. R., Muzzin, A., Franx, M., & Marchesini, D. 2017, ApJ, 849, L26
Johnson, H. L., Harrison, C. M., Swinbank, A. M., et al. 2018, MNRAS, 474, 5076
Jones, G. C., Vergani, D., Romano, M., et al. 2021, MNRAS, 507, 3540
Kassin, S. A., Weiner, B. J., Faber, S. M., et al. 2007, ApJ, 660, L35
Kassin, S. A., Weiner, B. J., Faber, S. M., et al. 2012, ApJ, 758, 106
Krumholz, M. R., Burkhart, B., Forbes, J. C., & Crocker, R. M. 2018, MNRAS, 477, 2716
Lang, P., Förster Schreiber, N. M., Genzel, R., et al. 2017, ApJ, 840, 92
Law, D. R., Steidel, C. C., Erb, D. K., et al. 2009, ApJ, 697, 2057
Lelli, F., Di Teodoro, E. M., Fraternali, F., et al. 2021, Science, 371, 713
Leroy, A. K., Walter, F., Brinks, E., et al. 2008, AJ, 136, 2782
Leroy, A. K., Walter, F., Bigiel, F., et al. 2009, AJ, 137, 4670
Livermore, R. C., Jones, T. A., Richard, J., et al. 2015, MNRAS, 450, 1812
Lovell, M. R., Pillepich, A., Genel, S., et al. 2018, MNRAS, 481, 1950
McMullin, J. P., Waters, B., Schiebel, D., Young, W., & Golap, K. 2007, in Astronomical Data Analysis Software and Systems XVI, eds. R. A. Shaw, F. Hill, & D. J. Bell, ASP Conf. Ser., 376, 127
Mogotsi, K. M., de Blok, W. J. G., Caldú-Primo, A., et al. 2016, AJ, 151, 15
Molina, J., Ibar, E., Smail, I., et al. 2019, MNRAS, 487, 4856
Navarro, J. F., Frenk, C. S., & White, S. D. M. 1996, ApJ, 462, 563
Neeleman, M., Prochaska, J. X., Kanekar, N., & Rafelski, M. 2020, Nature, 581, 269
Ostriker, E. C., & Shetty, R. 2011, ApJ, 731, 41
Price, S. H., Shimizu, T. T., Genzel, R., et al. 2021, ApJ, 922, 143
Riechers, D. A., Bradford, C. M., Clements, D. L., et al. 2013, Nature, 496, 329
Rizzo, F., Vegetti, S., Powell, D., et al. 2020, Nature, 584, 201
Rizzo, F., Vegetti, S., Fraternali, F., Stacey, H. R., & Powell, D. 2021, MNRAS, 507, 3952

Rubin, V. C., & Ford, W. K., Jr. 1970, ApJ, 159, 379
Simons, R. C., Kassin, S. A., Weiner, B. J., et al. 2017, ApJ, 843, 46
Smit, R., Bouwens, R. J., Carniani, S., et al. 2018, Nature, 553, 178
Sofue, Y., & Rubin, V. 2001, ARA&A, 39, 137
Stott, J. P., Swinbank, A. M., Johnson, H. L., et al. 2016, MNRAS, 457, 1888
Swinbank, A. M., Papadopoulos, P. P., Cox, P., et al. 2011, ApJ, 742, 11
Tacconi, L. J., Neri, R., Genzel, R., et al. 2013, ApJ, 768, 74
Tacconi, L. J., Genzel, R., Saintonge, A., et al. 2018, ApJ, 853, 179
Tacconi, L. J., Genzel, R., & Sternberg, A. 2020, ARA&A, 58, 157
Turner, O. J., Cirasuolo, M., Harrison, C. M., et al. 2017, MNRAS, 471, 1280
Übler, H., Genzel, R., Tacconi, L. J., et al. 2018, ApJ, 854, L24
Übler, H., Genzel, R., Wisnioski, E., et al. 2019, ApJ, 880, 48
Wisnioski, E., Förster Schreiber, N. M., Wuyts, S., et al. 2015, ApJ, 799, 209
Wisnioski, E., Förster Schreiber, N. M., Fossati, M., et al. 2019, ApJ, 886, 124
Wuyts, S., Förster Schreiber, N. M., Wisnioski, E., et al. 2016, ApJ, 831, 149

Appendix A: DYSMAL analysis

As described in Section 3.3, we modeled the kinematics of HZ4 using the DYSMAL code (Cresci et al. 2009; Davies et al. 2011; Wuyts et al. 2016; Price et al. 2021). DYSMAL explores the parameter space based on a MCMC sampling using the EMCEE package (Foreman-Mackey et al. 2013). Our model assumes a thick, turbulent disk embedded in a dark matter halo that follows a Navarro-Frenk-White (NFW) profile (Navarro et al. 1996), and it has a halo mass $M_{\rm halo}$ and a concentration parameter $c_{\rm halo}$. For the galaxy, we assume an exponential disk with effective radius $R_{\rm e}$. These are reasonable assumptions based on the analysis of the integrated [C II] line emission in Paper I. DYSMAL calculations are based on the assumed shape of the baryon distribution. Then the code differentiates between the circular velocity from the baryon distribution and the NFW profile. We also assume an intrinsic velocity dispersion σ_0 that is constant and isotropic throughout the disk. The model includes an asymmetric drift correction to the model circular velocity due to pressure support following Burkert et al. (2010).

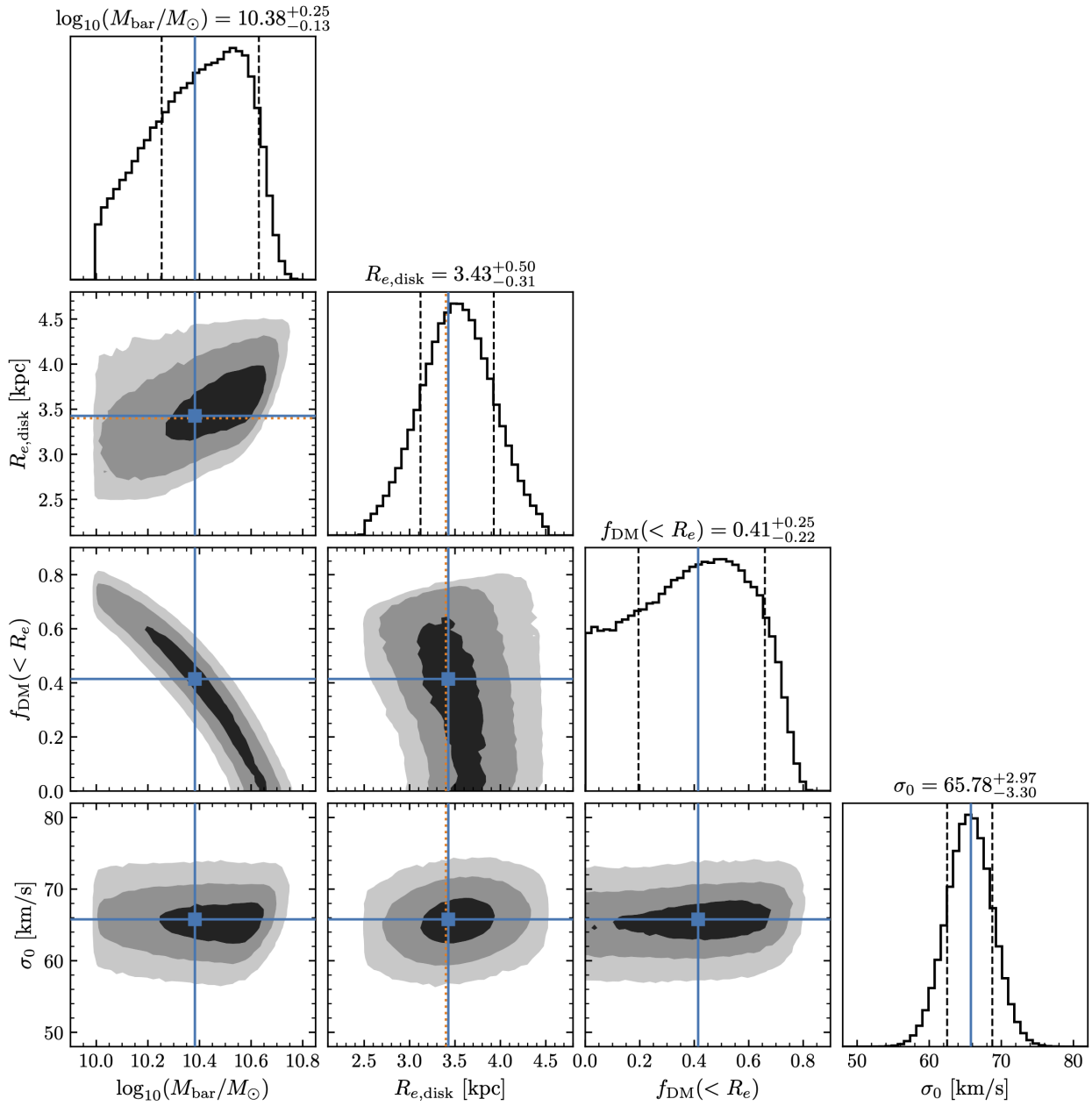

Fig. A.1. MCMC "corner plot" for the kinematic modeling of HZ4. Figure shows the 1D and 2D projections of the posterior probability distributions of the four free parameters: the total baryonic mass ($M_{\rm bar}$), the effective radius ($R_{\rm e}$), the dark-matter fraction within one effective radius ($f_{\rm DM}(\leq R_{\rm e})$), and the intrinsic velocity dispersion (σ_0). For Gaussian priors, the centers are marked with orange lines. The maximum a posteriori values of each parameter (found by jointly analyzing the posteriors of all parameters; the "best-fit" values) are shown with blue squares and lines. For the 2D histograms, the contours correspond to the 1, 2, and 3σ confidence intervals. For the 1D histograms, the uncertainties are the shortest interval enclosing or 1σ of the marginalized posterior distribution.

Free parameters in our modeling are the total baryonic mass ($M_{\rm bar}$), the effective radius ($R_{\rm e}$), the intrinsic velocity dispersion (σ_0), and the enclosed dark-matter fraction within one effective radius ($f_{\rm DM}(R_{\rm e})$). The latter was measured as the squared ratio between the dark matter ($v_{\rm circ,DM}$) and total ($v_{\rm circ,tot}$) intrinsic circular velocities measured at $R_{\rm e}$, that is $f_{\rm DM}(R_{\rm e}) = v^2_{\rm circ,DM}(R_{\rm e})/v^2_{\rm circ,tot}(R_{\rm e})$. For the total baryonic mass, we chose a Gaussian prior bounded in the range $\log_{10}(M_{\rm bar}/M_\odot) \in [10, 11.5]$ dex with a standard deviation of 0.2 dex, and centered at the expected baryonic mass derived from the sum of the stellar ($M_\star = 10^{10.15}\,M_\odot$; Faisst et al. 2020) and gas mass assuming a gas fraction of $M_{\rm gas}/M_\star = 0.75$ (e.g., Dessauges-Zavadsky et al. 2020). For the effective radius, we also assumed a Gaussian prior bounded in the range $R_{\rm e} \in [2.5, 4.5]$ kpc and centered at a value of $R_{\rm e} = 3.4$ kpc following the results from Paper I. For the intrinsic velocity dispersion and the dark-matter fraction, we adopted flat bounded priors of $\sigma_0 \in [20, 100]\,{\rm km\,s^{-1}}$ and $f_{\rm DM}(R_{\rm e}) \in [0, 1]$, respectively. Given the difficulty of simultaneously fitting for more parameters due to the resolution and signal-to-noise (S/N) of the data, we fixed: (1) the kinematic center and position angle, as described in Section 3.1; (2) the inclination to $i = 52°$, based on the morphology of the ALMA [C II] line data (Paper I) and assuming a ratio of scale height to scale length with a thickness = 0.15; and (3) the halo concentration parameter, $c_{\rm halo} = 2.3$, typical for the redshift and halo mass of HZ4 according to Dutton & Macciò (2014).

The MCMC code was run using 800 walkers, a burn-in phase of 800 steps, and a running phase of 5000 steps. Figure A.1 shows the MCMC sampling of the joint posterior probability distribution (or "corner plot"). The best-fit model from the MCMC analysis is shown with a black solid line on top of the rotation curve and velocity dispersion profile in Fig. 1. In addition, Fig. A.2 shows the position-velocity diagram of HZ4 and the resulting best-fit DYSMAL model cube extracted along the major (PA = 200°) and minor kinematic axes.

If we varied the assumption of the inclination by ±10%, we observed a similar variation in the derived baryonic mass and the dark-matter fraction. Also, if we fixed $R_{\rm e} = 3.4$ kpc (Paper I), and let the inclination free with a Gaussian prior centered at $i = 52°$ and bounded in the range $i \in [30°, 70°]$, then the model-derived inclination results $i = 51.9°^{+5.6}_{-10.7}$, and the dark-matter fraction was $f_{\rm DM}(R_{\rm e}) = 0.45^{+0.19}_{-0.28}$, consistent with the results from the fixed-inclination model.

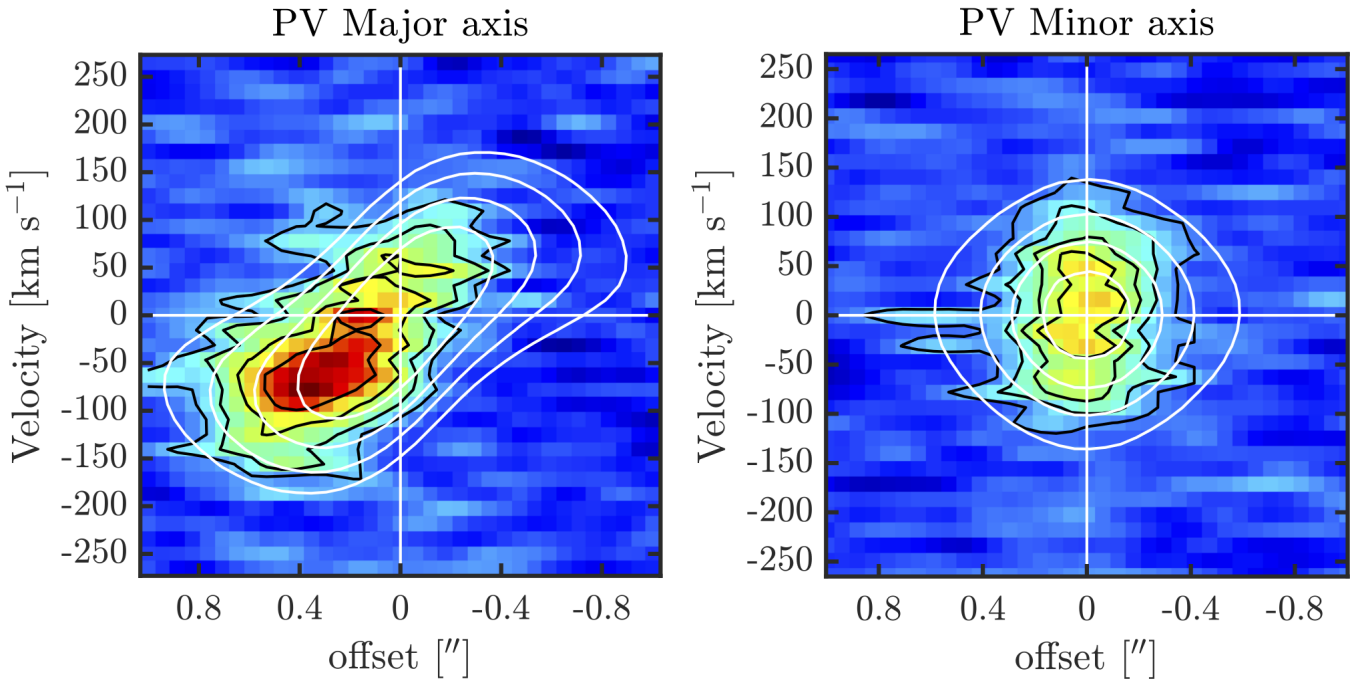

Fig. A.2. Position-velocity diagrams of HZ4 extracted along the major (left panel, PA = 200°) and minor (right panel) kinematic axis using a pseudo-slit of 0.4″ width. The black contours in the left panel show 3, 5, 8, and 10σ contours (1σ = 0.1 mJy beam^{-1}), and in the right panel they represent 2, 4, 6, and 8σ contours. The white contours show the best-fit DYSMAL model at corresponding similar contour levels.